Journal Pre-proof

A new type of magnetic field arrangement to suppress meniscus fluctuation in slab casting: Numerical simulation and experiment

Yang Li, Anyuang Deng, Lintao Zhang, Bin Yang, Engang Wang

PII: S0924-0136(21)00238-7

DOI: https://doi.org/10.1016/j.jmatprotec.2021.117278

Reference: PROTEC 117278

To appear in: *Journal of Materials Processing Tech.*

Received Date: 24 September 2020

Revised Date: 15 June 2021

Accepted Date: 23 June 2021

Please cite this article as: { doi: https://doi.org/

This is a PDF file of an article that has undergone enhancements after acceptance, such as the addition of a cover page and metadata, and formatting for readability, but it is not yet the definitive version of record. This version will undergo additional copyediting, typesetting and review before it is published in its final form, but we are providing this version to give early visibility of the article. Please note that, during the production process, errors may be discovered which could affect the content, and all legal disclaimers that apply to the journal pertain.

© 2020 Published by Elsevier.

Journal Pre-proof

A new type of magnetic field arrangement to suppress meniscus fluctuation in slab casting: numerical simulation and experiment

Yang Li[a,b], Anyuang Deng[a,b,*], Lintao Zhang[c], Bin Yang[a,b], Engang Wang[a,b]

[a]*Key Laboratory of Electromagnetic Processing of Materials, Ministry of Education, Northeastern University, No. 3-11, Wen Hua Road, Shenyang 110004, China.*
[b]*School of Metallurgy, Northeastern University, No. 3-11, Wen hua Road, Shenyang 110004, China.*
[c]*Future Manufacturing Research Institute, College of Engineering, Swansea University, Bay Campus, Fabian Way, Swansea SA1 8EN, UK.*

Abstract

This research aimed at proposing a new type of magnetic field arrangement to suppress the meniscus fluctuation in slab continuous casting. The work was conducted by three dimensional (3D) numerical simulation and followed by an experiment validation. The results indicated that the maximum height of meniscus was decreased and the meniscus fluctuation was decreased significantly whilst the applied magnetic field was increased from 0 to 0.05 T. The surface velocity was not sensitive to the applied magnetic field magnitude to 0.05 T. The results obtained from the designed experiment had a good agreement with the simulation results: this is an indication of the effectiveness of the proposed magnetic field arrangement.

Keywords: Metallurgy, Slab casting, Meniscus fluctuation, Electromagnetic field, Volume of fluid

1. Introduction

In the continuous casting process, the slab casting mould system is special because it consists a submerged entry nozzle (SEN). SEN is adopted as a chan-

*Corresponding author
URL: dengay@epm.neu.edu.cn (Anyuang Deng)

Journal Pre-proof

Journal Pre-proof

nel to deliver the melt from tundish/ladle to the slab mould. The SEN jet flow usually generates an upward flow towards the meniscus and a downward flow to the mould exit (along casting direction). These two part flows are separated by an impingement point on the narrow face (NF) of the slab mould. The upward flow attracts more attention because it is highly related with the meniscus behaviour. Meniscus fluctuation can result in a series of severe problems therefore to worsen the slab quality, e.g. the slag entrapments.

One way to reduce meniscus fluctuations is to weaken the upward flow. This can be achieved by pushing the SEN jet flow towards mould exit. This can be achieved simply by increasing SEN immersion depth and/or adopting downward SEN port. Thomas et al. (2015a) studied the influence of SEN immersion depth on the meniscus fluctuations (represented by the surface velocity): the results showed that the meniscus turbulence was decreased significantly whilst the depth increased from 0.185 to 0.365 m. Similar results were obtained by Miranda et al. (2005): the immersion depth increased from 0.05 to 0.09 m, the meniscus became flat and the fluctuation was suppressed. Jim et al. (2017) also investigated the influence of the SEN immersion depth and the results indicated that the surface velocity decreased significantly as the depth values increased from 0.17 to 0.2 m. Gupta & Lahiri (1994) studied the influence of the upward SEN port (positive angle value) and the downward SEN port (negative angle value) on the meniscus behaviour. The results indicated that the port angle varied from an upward angle (15^o) to a downward angle (-25^o), the meniscus fluctuation amplitude decreased by 50%. Similarly, a more uniform velocity distribution on meniscus along the wide face (WF) of the mould was achieved whilst the port angle varied from 15^o to -30^o, as reported by Cho et al. (2019). However, the above methods, increasing SEN immersion depth and adopting the downward SEN port, could push the melt too deep to the mould and affect the flotation of inclusions. Additionally, those methods also require a longer slab mould to avoid the accidents like 'breakout'.

The electromagnetic brake (EMBr) technique is also an effective method to control the meniscus fluctuation. EMBr technique has been applied in industry,

Journal Pre-proof

as reported by Lehman et al. (1996). Hwang et al. (1997) studied the effect of EMBr and pointed out that a proper magnetic field could suppress the meniscus fluctuation. However, too strong magnetic field could enhance meniscus fluctuation. This was because the jet deflected upwards to avoid the strong field region, and may disrupt the top surface, especially in wide slabs. The principles of this phenomenon are identical to the other flow behaviour, e.g. the backward facing step (Armaly et al. (1983)), the flow past cylinder under a high magnetic field (Dousset & Potherat (2008)) and the flow past the sharp bends (Zhang & Potherat (2013)). Ha et al. (2003) investigated the flow field and the temperature distribution in the mould at different applied magnetic fields. The results indicated that the maximum flow velocity underneath the meniscus decreased 63.3% whilst the applied magnetic field was 0.3 T at the casting velocity was 1.8 m/min. Yu et al. (2008) studied the influence of the locations of the EMBr core region on the flow velocity near meniscus. The results showed that the control effect could be less effective as the EMBr core departing to the meniscus. Further, Singh et al. (2013) set up a model to simulate the EMBr effect on the flow turbulence in the slab mould. The influence of conductive mould walls was also discussed and the results unveiled that the magnetic field could deflect the jet flow towards the meniscus. This increased the surface velocity of meniscus from 0.07 to 0.25 m/s, compared to the case without magnetic field. Thomas et al. (2015b) concluded that to lower of the magnetic field, e.g. below the SEN port, could reduce the surface flow velocity and to achieve a stable meniscus. Recently, a new type of EMBr was proposed by Li et al. (2017) and the vertical magnetic poles could stabilize the flow in the vicinity of narrow face of the slab mould effectively. It showed that EMBr could reduce the upward flow to reduce the meniscus fluctuation. By adopting EMBr system, the flow control can be achieved, e.g. the multi-mode EMBr system, however, there are still some limitations to its wide application: the system is complex and requires more space to assembly; the suppressed upward flow can result in the temperature decrease near the meniscus region, especially under low casting speed. The advanced meshless method was also adopted to model both EMBr and electromagnetic

Journal Pre-proof

Journal Pre-proof

stirring (EMS) processes, as discussed by Mramor et al. (2015) and Vertnik et al. (2019), respectively. The results indicated that the meshless method can achieve high accuracy results even for a complex flow: the liquid metal under magnetic field in the mould, for instance.

The current proposed method aims to suppress the meniscus fluctuation through the magnetic pressure, which is inspired by the electromagnetic continuous casting technique (Vives & Ricou (1985)). The novelty of the work is that a new type of magnetic field arrangement is proposed: the high frequency magnetic field is placed above the narrow face of the slab mould where the meniscus fluctuates most due to SEN upward jet flow. This has never been reported before, according to the authors' knowledge. There are several open questions for the current proposed method:

1. Will the proposed method suppress the meniscus fluctuations? Will a simpler system to control the meniscus turbulence, compared to EMBr system, can be achieved?
2. How does the proposed method (Joule heat is involved) influence the melt temperature near meniscus?

In the current work, we only focus on the first question and the second will be discussed in the following work. A numerical model based on the two-way coupled analysis between flow field and magnetic field was set up. The modelling work is followed by a self-designed experiment as a further validation. The outline of paper is as follows. The basic principle of the proposed method is discussed in Sec.2. The configuration used for the modelling is proposed in Sec.3.1. The numerical set-up for the magnetic and flow modelling are discussed in Sec. 3.2.1 and 3.2.2. In the modelling results Sec.4, the magnetic feature of the system, the meniscus behaviour and the flow field are investigated in Sec.4.1, 4.2 and 4.3, respectively. The experimental results are studied in Sec.5. The main conclusions are summarized in Sec.6.

Journal Pre-proof

Journal Pre-proof

2. Basic principle

The Young-Laplace equation expresses:

$$\Delta p = -\gamma \nabla \cdot \hat{\mathbf{n}}, \tag{1}$$

where Δp, γ and $\hat{\mathbf{n}}$ are the Laplace pressure, the surface tension and the unit vector normal to the surface, respectively. This equation is used to describe the capillary pressure difference sustained across the interface between two static fluids. Equation 1 can be further simplified as:

$$\Delta p = -\gamma(\frac{1}{R_1} + \frac{1}{R_2}), \tag{2}$$

where R_1 and R_2 are the principal radii of curvatures. For a steady free surface, the forces are balanced between the external applied pressure, the hydrostatic pressure and the surface tension effect:

$$\Delta p = \rho g h - \gamma(\frac{1}{R_1} + \frac{1}{R_2}), \tag{3}$$

where g and h are the gravitational constant and the relative height. For a static free surface under magnetic field, as reported by Negrinia et al. (2000), the Equation 3 can be rewritten as:

$$p_m = \rho g h - \gamma(\frac{1}{R_1} + \frac{1}{R_2}), \tag{4}$$

where p_m denotes a time averaged magnetic pressure force on a given area.

For the current case, a transient free surface, under the magnetic pressure, Equation 4 can be further modified as:

$$\frac{\rho \mathbf{v}^2}{2} + p_m = \rho g h - \gamma(\frac{1}{R_1} + \frac{1}{R_2}), \tag{5}$$

where $\mathbf{v}$ is the velocity of the melt. The electromagnetic force in alternating magnetic field can be written as:

$$\mathbf{F}_{mag}(r) = \mathbf{J}(\mathbf{r}) \times \mathbf{B}(\mathbf{r}), \tag{6}$$

where $\mathbf{F}_{mag}$ and $\mathbf{r}$ are the electromagnetic body force and the unit vector pointing to the normal direction of the meniscus. $\mathbf{J}$ and $\mathbf{B}$ are the induced current

Journal Pre-proof

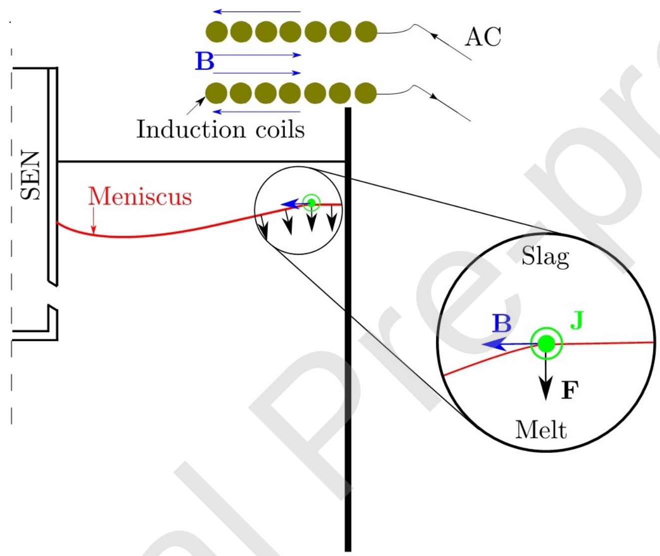

Figure 1: Basic principle of the proposed method (two-dimensional front view). The force **F** is generated by the interaction of induced current **J** and the magnetic field **B**. Both **J** and **B** are produced by the applied high frequency alternating current (AC).

Journal Pre-proof

and the magnetic flux density, as showed in Fig.1. Equation 6 can be further simplified as:

$$\mathbf{F}_{mag} = -\nabla\frac{|\mathbf{B}|^2}{2\eta} + \frac{(\mathbf{B}\cdot\nabla)\mathbf{B}}{\eta}, \tag{7}$$

where η is the magnetic permeability. Under the high frequency condition, e.g. 8 kHz, the second term of Equation 7 can be neglected. Therefore to rewrite Equation 5 as:

$$\frac{\rho\mathbf{v}^2}{2} + \frac{|\mathbf{B}|^2}{2\eta} = \rho gh - \gamma(\frac{1}{R_1} + \frac{1}{R_2}). \tag{8}$$

The current proposed method generates an external magnetic pressure ($\frac{|\mathbf{B}|^2}{2\eta}$) with an aim to vary the values of R_1 and R_2 (to control the shape of meniscus).

3. Configuration and numerical set-up

3.1. Configuration

Fig.2 showed the configuration adopted in the numerical simulation. Due to symmetry feature, only half of the system was modelled. The origin of the frame O and the coordinate system were presented. The directions paralleled to the slab mould wide face (WF), the casting direction and narrow face (NF) are defined as x-axis, y-axis and z-axis, respectively. The inner diameter of the SEN was 0.07 m. D_{sen}, defined as the SEN immersion depth, is 0.235 m. The slag layer had a thickness of 0.05 m. A 10-turn hollow copper induction coils were placed on the top, near the NF. The hollow cavity was used as the cooling channel. A single phase harmonic current with a frequency of 8 kHz was applied to the coils. The SEN and the slag layer were only involved in the fluid flow modelling. The detailed model parameters and operating conditions are summarized in Tab.1.

3.2. Numerical set-up

The following assumptions were made:

1. The problem was isothermal;

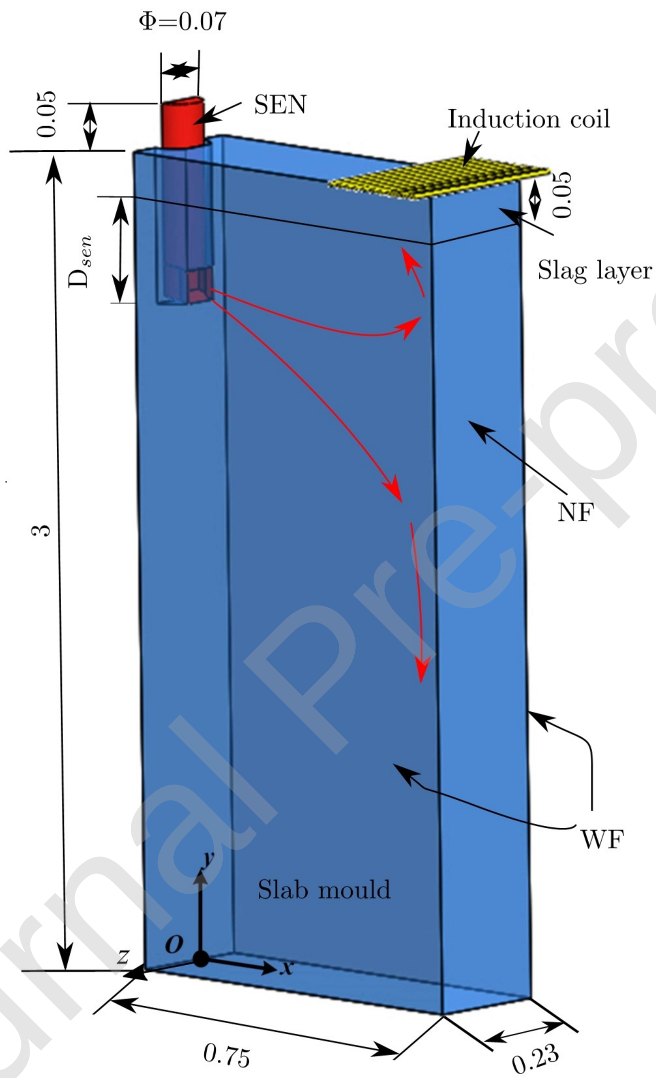

Figure 2: Configuration adopted in modelling. Unit is in meter. D_{sen} is defined as the immersion depth of submerged entry nozzle (SEN). The induction coils (10-turn) is placed on the top the mould, near the narrow face of the slab mould.

Journal Pre-proof

Journal Pre-proof

Table 1: Parameters and operating conditions.

Parameter	Value
Immersion depth of SEN (D_{SEN}), m	0.235
Port angle of SEN (θ_p), deg	-15
Casting speed, m/min	1.6
Density of molten steel, $kg \cdot m^{-3}$	7200
Viscosity of molten steel, $kg \cdot m^{-1} \cdot s$	0.006
Density of slag, $kg \cdot m^{-3}$	3500
Viscosity of slag, $kg \cdot m^{-1} \cdot s$	0.2
Electric conductivity of molten steel, $S \cdot m^{-1}$	7.14×10^5
Operating frequency, kHz	8
Surface tension between molten steel and slag, N/m	1.15
Relative permeability of the molten steel and slag, -	1

2. Only the liquid slag layer was considered, the air phase and the other state slag layers were neglected;
3. The molten steel and liquid slag were considered to be homogeneous, viscous and incompressible fluid;
4. The influence of the initial solidified shell and the mould oscillation were ignored;
5. The physical properties of molten steel and liquid slag were constant and isotropic;
6. The effect of molten steel flow on electromagnetic field was ignored.

3.2.1. Electromagnetic field modelling

The electromagnetic numerical simulation was conducted by using ANSYS® Mechanical APDL. The electromagnetic field was controlled by the Maxwell equations. An air box, surrounding the mould and coils, was drawn as the outer boundary. Zero magnetic potential boundary condition along x, y, and z

Journal Pre-proof

Journal Pre-proof

direction (A_x=0, A_y=0, A_z=0) were employed on its external surfaces, where $\mathbf{A}$ is the magnetic potential: $\nabla \times \mathbf{A} = \mathbf{B}$.

3.2.2. Flow field modelling

The flow simulations were conducted by using ANSYS® FLUENT. The slag/steel interface positions were traced by volume of fluid (VOF) method. For the current case, two phases were involved: the slag and steel. The continuity equation for mixture phase can be expressed as:

$$\frac{\partial \rho_m}{\partial t} + \nabla \cdot (\rho_m \mathbf{u}_m) = 0, \tag{9}$$

where ρ_m and $\mathbf{u}_m$ denote the mixture density and velocity. The volume fraction equation for molten steel can be written as:

$$\frac{\partial \alpha_{st}}{\partial t} + \nabla \cdot (\alpha_{st} \mathbf{u}_{st}) = 0, \tag{10}$$

where α_{st}, $\mathbf{u}_{st}$ stand for the volume fraction and velocity, respectively. In a single cell, the steel volume fraction is constrained by the following equation:

$$\alpha_{st} + \alpha_{sl} = 1, \tag{11}$$

where α_{sl} is the slag phase volume fraction.

A single momentum equation was solved throughout the computing domain. The velocity field was shared by two phases. The momentum equation was depended on the volume fractions of two phases through the following equation:

$$\frac{\partial(\rho_m \mathbf{u}_m)}{\partial t} + \nabla \cdot (\rho_m \mathbf{u}_m \mathbf{u}_m) = -\nabla p + \nabla \cdot [(\mu_m + \mu_t)(\nabla \mathbf{u}_m + \nabla \mathbf{u}_m^T)] + \rho \mathbf{g} + \mathbf{f}_\sigma + \mathbf{F}_{mag}, \tag{12}$$

where p, μ_m, μ_t, $\mathbf{f}_\sigma$ and $\mathbf{F}_{mag}$ are the pressure, the dynamic viscosity of the mixture, the turbulence viscosity, the surface tension and the electromagnetic force, respectively. The standard $k - \epsilon$ model was applied to describe turbulence feature of the flow in the mould. This model has already been validated to describe the mould flow by Kim et al. (2000). The transport equation of turbulent kinetic energy and its dissipation rate were solved to obtain the effective

Journal Pre-proof

viscosity:

$$\frac{\partial}{\partial t}(\rho_m k) + \nabla \cdot (\rho_m \mathbf{u}_m k) = \nabla \cdot (\mu_m + \frac{\mu_t}{\sigma_k})\nabla k + G - \rho_m \epsilon \tag{13}$$

and

$$\frac{\partial}{\partial t}(\rho_m \epsilon) + \nabla \cdot (\rho_m \mathbf{u}_m \epsilon) = \nabla \cdot (\mu_m + \frac{\mu_t}{\sigma_\epsilon})\nabla \epsilon + \frac{\epsilon}{k}(C_1 G - C_2 \rho_m \epsilon) \tag{14}$$

where k and ϵ are turbulent kinetic energy and turbulent dissipation rate, respectively. $C_1, C_2, \sigma_k, \sigma_\epsilon$ are the empirical constants and its value are 1.38, 1.92, 1.0 and 1.3, respectively. G is the generation of turbulent kinetic energy due to the mean velocity gradient.

The Continuum Surface Force (CSF) model proposed by Brackbill was adopted for the description of surface tension (Brackill et al. (1991)). It can be expressed as:

$$\mathbf{f}_\sigma = 2\gamma \frac{\rho_m \kappa \nabla \alpha_{st}}{\rho_{st} + \rho_{sl}}, \tag{15}$$

and

$$\kappa = -\nabla \cdot \frac{\nabla \alpha_{st}}{|\nabla \alpha_{st}|}, \tag{16}$$

where where κ stands for the curvature and is defined in terms of the divergence of the unit vector.

Fig.3 and Fig.4 showed the adopted boundary conditions along the meshes (3D view) and the meshes on $x - y$ plane at z=0 m (2D view). The velocity boundary condition was used at the inlet (IN) with a direction of $-y$ axis. The magnitude of the velocity was calculated by using casting velocity, based on mass conservation. The outflow boundary condition was applied on the outlet plane (OUT), where the diffusion flux of all flow variables vertical the outlet (along $-y$-axis direction) was zero. The non-slip boundary condition was adopted for the narrow face (NF) and the wide face (WF) of the slab mould. The free slip boundary condition was used for the top surface (TS), which denotes the velocity gradient on the plane was zero. This is a universal simplified method ignoring air phase for numerical model and used in many literatures: the work of Li et al. (2020); Xu et al. (2018); Sun et al. (2018), for instance. The symmetry

Journal Pre-proof

Journal Pre-proof

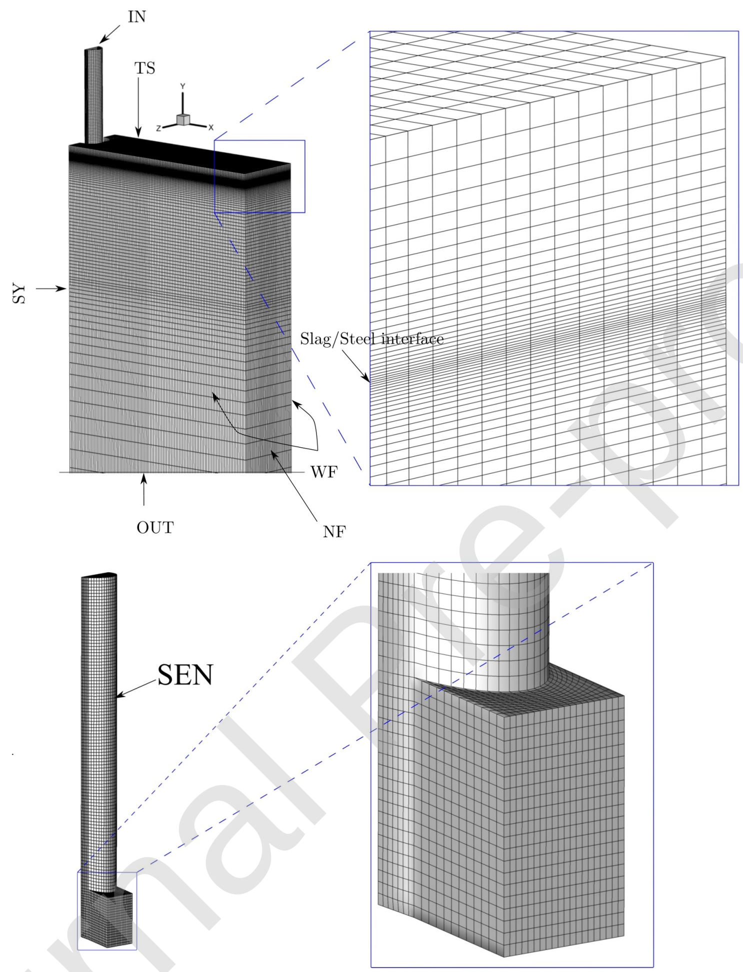

Figure 3: Surfaces used to apply boundary conditions (*Top-Left*) and part of meshes in the domain (*Top-Right*). IN, OUT, SY, NF WF and TS stand for the inlet, the outlet, the symmetric plane, the narrow face, the wide face and the top surface, respectively. The minimum cell dimension along y direction is 0.1 mm in the vicinity of the slag/steel interface. The meshes of SEN (*Bottom-Left*) and the outlet of SEN (*Bottom-Right*) are given ,respectively. The edge length of the element in vicinity of the SEN out is 5 mm.

Journal Pre-proof

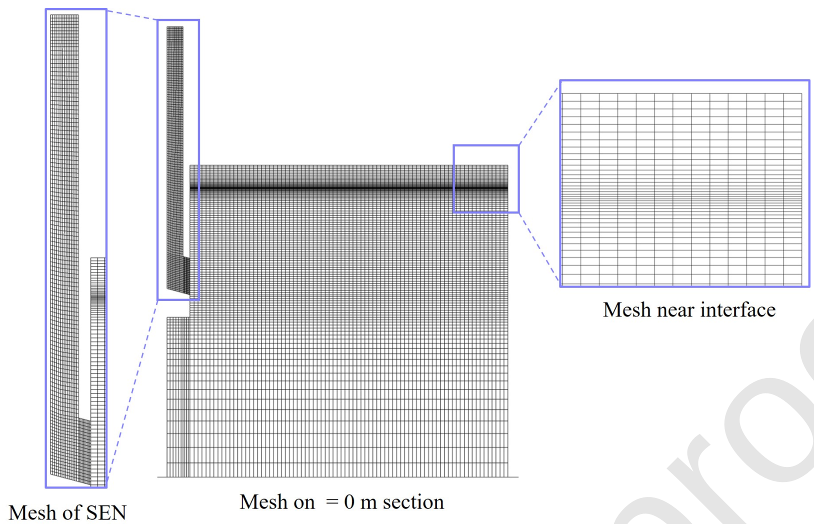

Figure 4: Mesh on $x-y$ plane at z=0 m.

boundary was used for the symmetric plane (SY) where the normal gradients of all variables were zero. PISO scheme was selected to couple the velocity and pressure. For the spatial discretization, the least-squares cell based, the PRESTO, the second-order upwind, and the Geo-reconstruct were used for the gradient, the pressure, the momentum, and the volume fraction, respectively. The first-order implicit method is used as the transient formulation.

In order to capture the feature of meniscus precisely, a mesh sensitive test was conducted and the results were summarized in Tab.2. The refined strategy was focused on the region of upward circulation and interface, where the meshes only along y direction were refined. In the table, ϵ_{h^a}, and ϵ_{h^b} are the errors of the highest and lowest meniscus locations. $\epsilon_{|\mathbf{u}|^a}$, $\epsilon_{u_x^a}$, $\epsilon_{u_x^b}$, $\epsilon_{u_y^a}$, $\epsilon_{u_y^b}$, ϵ_{k^a}, $\epsilon_{\Delta h}$ and ϵ_f denote the errors of the maximum velocity magnitude, the maximum u_x value, the minimum u_x value, the maximum u_y value, the minimum u_y value, the maximum turbulence kinetic energy value along the selected line, between point (0.375, 2, 0) and point (0.375, 2.95, 0), the meniscus fluctuations and the interface oscillation frequency, respectively. The oscillation frequency of

Journal Pre-proof

Table 2: Main characteristics of the different meshes and errors (ϵ). In the table, the superscript a and b denote the maximum and minimum values of specified variables. The values are time averaged in 5 s ($\sim$ 16-fluctuation periods). In the table, i refers to the mesh number in the range of 1 to 4. Mesh3 is the adopted mesh and Mesh4 is the benchmark mesh.

	Mesh1	Mesh2	Mesh3	Mesh4
Total element number	417954	523242	591050	762486
$\epsilon_{h^a} = \lvert 1 - h^a(M_i)/h^a(M_4) \rvert$	4.70×10^{-5}	2.25×10^{-5}	5.76×10^{-6}	-
$\epsilon_{h^b} = \lvert 1 - h^b(M_i)/h^b(M_4) \rvert$	5.13×10^{-4}	4.35×10^{-4}	3.82×10^{-4}	-
$\epsilon_{\lvert\mathbf{u}\rvert^a} = \lvert 1 - \lvert\mathbf{u}\rvert^a(M_i)/\lvert\mathbf{u}\rvert^a(M_4) \rvert$	7.27×10^{-2}	1.61×10^{-2}	1.17×10^{-2}	-
$\epsilon_{u_x^a} = \lvert 1 - u_x^a(M_i)/u_x^a(M_4) \rvert$	2.88×10^{-2}	9.14×10^{-3}	7.71×10^{-3}	-
$\epsilon_{u_x^b} = \lvert 1 - u_x^b(M_i)/u_x^b(M_4) \rvert$	2.61×10^{-3}	5.74×10^{-3}	1.12×10^{-3}	-
$\epsilon_{u_y^a} = \lvert 1 - u_y^a(M_i)/u_y^a(M_4) \rvert$	9.54×10^{-1}	2.57×10^{-1}	4.65×10^{-2}	-
$\epsilon_{u_y^b} = \lvert 1 - u_y^b(M_i)/u_y^b(M_4) \rvert$	5.45×10^{-2}	1.7×10^{-2}	3.26×10^{-3}	-
$\epsilon_{k^a} = \lvert 1 - k^a(M_i)/k^a(M_4) \rvert$	2.35×10^{-2}	6.23×10^{-3}	3.11×10^{-3}	-
$\epsilon_{\Delta h} = \lvert 1 - \Delta h(M_i)/\Delta h(M_4) \rvert$	2.46×10^{-1}	2.10×10^{-1}	5.70×10^{-2}	-
$\epsilon_f = \lvert 1 - f(M_i)/f(M_4) \rvert$	5.00×10^{-1}	0	0	-

Journal Pre-proof

Journal Pre-proof

interface and the time-average meniscus fluctuation, at B_{max}=0.05 T, also were chosen as the criteria of mesh independence analysis. Mesh3 was adopted and this ensures good precision at a reasonable computational cost.

3.2.3. Numerical procedures

The two-way coupled analysis, presented by Spitans et al. (2013), was adopted. The detailed procedures were showed in Fig.5. The data transmission between

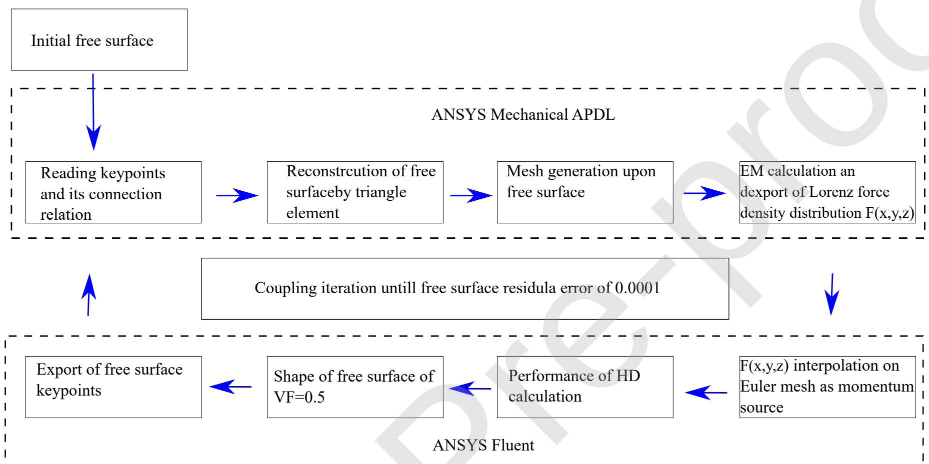

Figure 5: Flow diagram of two-way coupling calculation.

two ways were relied on a user defined function (UDF). The triangle element was chosen as the based surface in the process of reconstructing the free surface in magnetic modelling. Due to the tiny distance between some key points, the degenerate triangles were prone to occur and caused difficulties in meshing process. Therefore, another UDF was written with C language based on Delaunay triangulation algorithm to overcome this: merging those key points and optimizing the connection relation of them.

4. Simulation results

In this section, we first discuss the electromagnetic features of the system, e.g. the electromagnetic force distribution. Because that is the external force

Journal Pre-proof

Journal Pre-proof

applied to suppress the meniscus, as discussed in Equation 8. We then discuss the meniscus fluctuation behaviour and it is represented by the variations of the slag/steel interface height (y coordinate). We finally discuss the flow features on the meniscus and in the sub-meniscus region.

4.1. Electromagnetic features

Fig.6 showed the distribution of magnetic flux density $\mathbf{B}$ (*Top*), the induced current $\mathbf{J}$ (*Middle*) and the electromagnetic force $\mathbf{F}_{mag}$ (*Bottom*) vectors, respectively. The results showed that with the interaction of $\mathbf{J}$ and $\mathbf{B}$, the electromagnetic force was generated (Eq. 6), as showed in Fig.6 (*Bottom*). The results indicated that the force had a normal direction to the meniscus, pointing inside the melt. This force mainly acted on the meniscus surface due to the skin effect under high frequency: 8 kHz. The penetration depth of magnetic flux density for the molten steel is around 6.6 mm. The reason for the selection of 8 kHz was based on our previous work (Li et al. (2021)). The effect of suppressing meniscus fluctuation is highly related with the applied frequency of AC: higher frequency can results in small value of skin depth and further confine the meniscus surface. This force acted on the bulge deformation region and the meniscus trended flat.

Fig.7 showed the electromagnetic force distribution on meniscus (x-z plane at y=2.95 m) at different B_{max}. For a given B_{max}, the force increased as approaching to the narrow face of the mould. This was due to the induction coils were placed near that location. As B_{max} was increased, the forces were increased as well. The results showed that the maximum electromagnetic force magnitude increase nearly 3 times (672997 N v.s. 222255 N) whilst B_{max} increased from 0.028 to 0.05 T. Interestingly, a reversed 'C-shape' force distribution was observed. This became more dominant at higher value of B_{max}, e.g. Fig.7 (d). To further understand this, the magnitudes of $\mathbf{F}_{mag}$, $\mathbf{J}$ and $\mathbf{B}$ along x-axis (mould width direction) at z=0.105 m (near the mould wide face) under different B_{max} were plotted, as showed in Fig.8 (*Top*), (*Middle*) and (*Bottom*), respectively. The magnitudes of $\mathbf{F}_{mag}$, $\mathbf{J}$ and $\mathbf{B}$ along x-axis at z=0 m (middle of

Journal Pre-proof

Journal Pre-proof

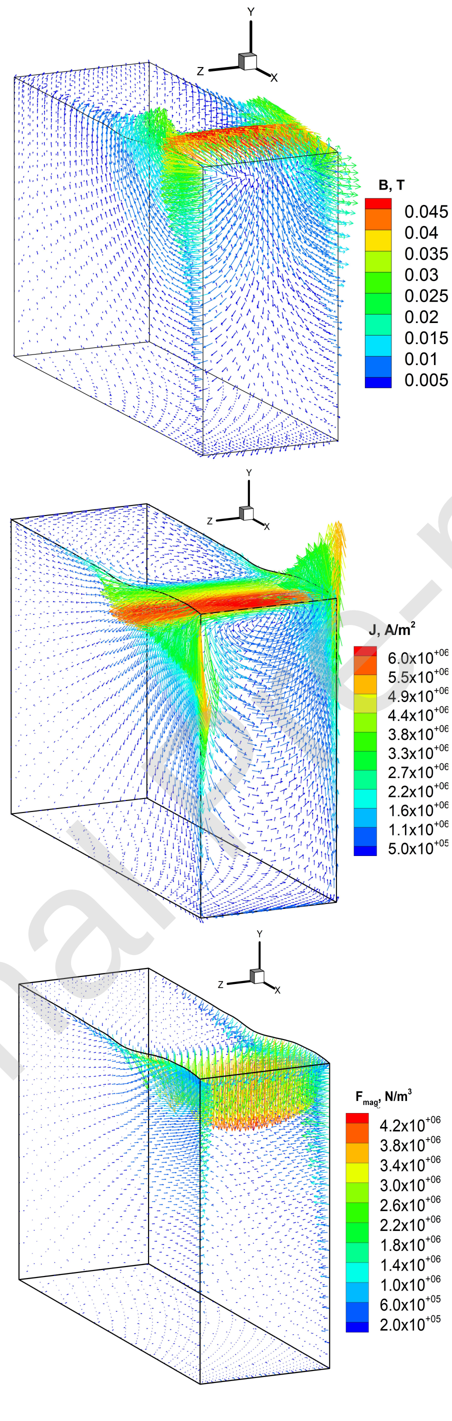

Figure 6: Vector distribution of magnetic flux density $\mathbf{B}$ (Top), the induced current $\mathbf{J}$ ($Middle$) and the electromagnetic force $\mathbf{F}_{mag}$ ($Bottom$). SEN is not included.

Journal Pre-proof

Journal Pre-proof

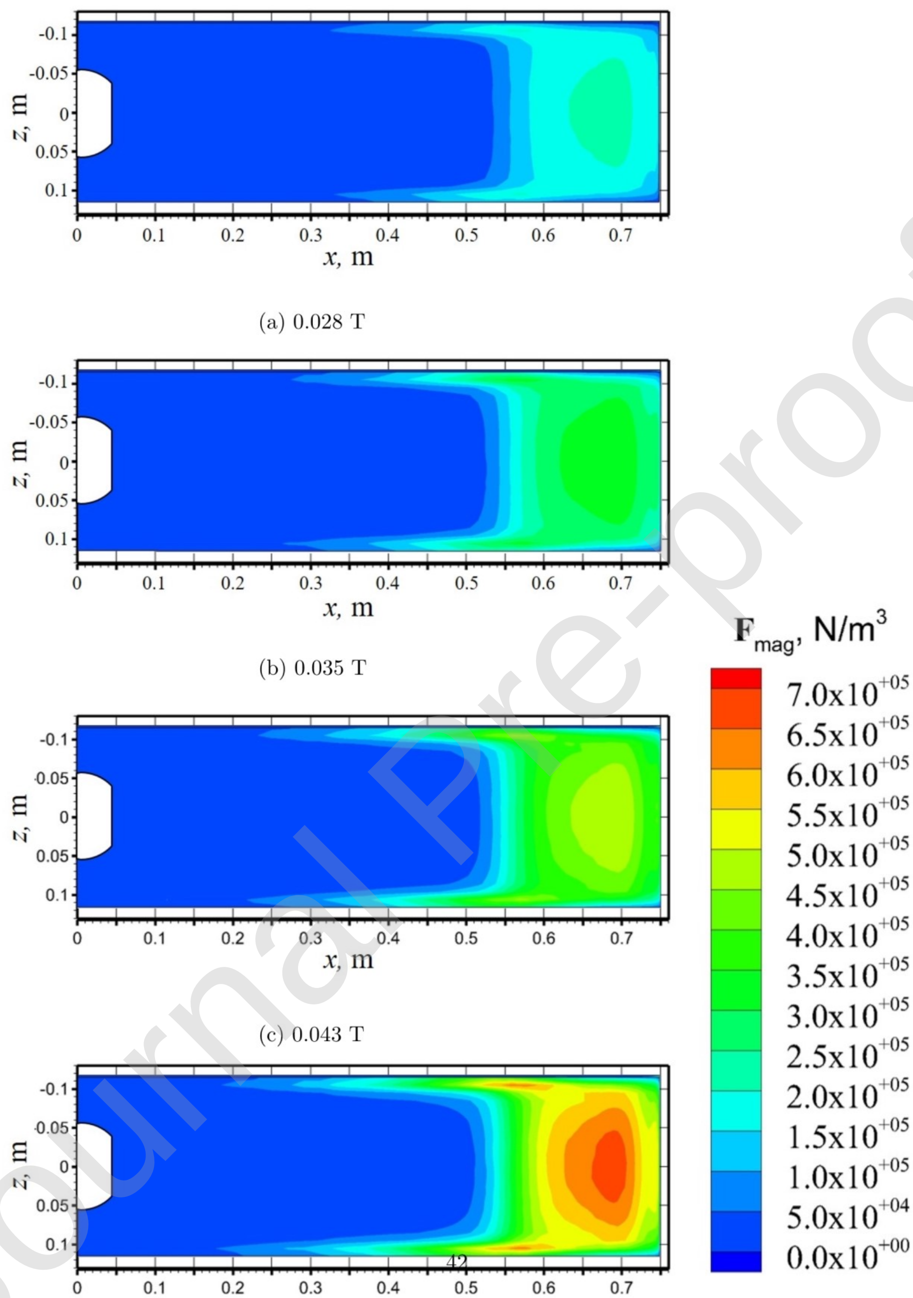

Figure 7: Electromagnetic force distribution on meniscus (x-z plane at y=2.95 m) at different applied magnetic field. B_{max} = 0.028 T (a), 0.035 T (b), 0.043 T (c) and 0.05 T (d). The magnitude of $\mathbf{F}_{mag}$ increases as B_{max} is increased. A reversed 'C-shape' distribution is observed.

Journal Pre-proof

Journal Pre-proof

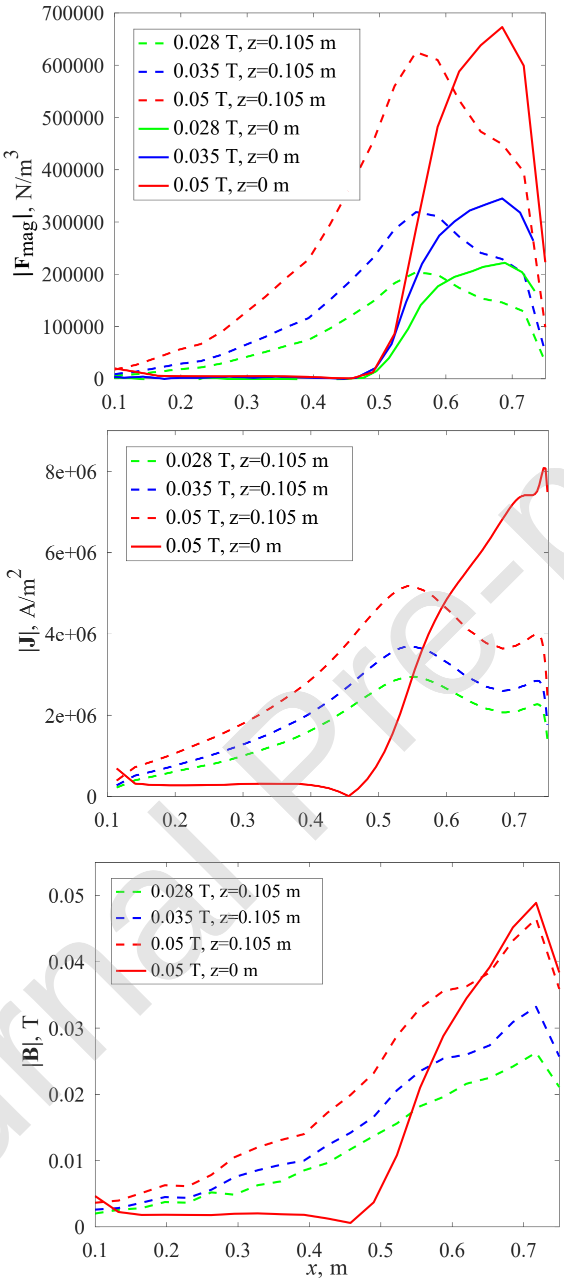

Figure 8: From top to bottom, magnitudes of $\mathbf{F}_{mag}$, $\mathbf{J}$, $\mathbf{B}$ plotted against $\mathbf{x}$ at different z for different B_{max}, receptively. The magnitudes increase as B_{max} is increased. For $|\mathbf{F}_{mag}|$ and $|\mathbf{J}|$, the locations where maximum value appear move towards SEN as the measured location is departing the central line of the slab mould ($z = 0$ m). $|\mathbf{B}|$ is not sensitive to this movement.

Journal Pre-proof

the slab mould across NF direction) were also plotted as benchmarks. In terms of the force distribution, as showed in Fig.8 (Top), the magnitude increased as B_{max} was increased, which agreed with the results obtained from Fig.7. However, it is observed that the locations where for maximum force magnitude were different. For example, this location moved from x=0.67 m to x=0.52 m whilst results plotted varied from z = 0 m and z = 0.105 m at B_{max} = 0.05 T. The main reason for this movement was due to the location where the maximum magnitude induced current appears was different, as showed in Fig.8 ($Middle$). This is mainly because that the induced current mainly concentrated on the surface under high frequency, e.g. 8 kHz, and a concentration appeared at the meniscus where close to the end location of the induction coils. This movement of **B** was not very sensitive to the results plotted location z, as showed in Fig.8 ($Bottom$), therefore, we can conclude that the reversed 'C-shape' distribution of the force was mainly due to the induced current concentration on the meniscus at the region below the induction coils.

4.2. Slag/steel interface behaviour

Fig.9 showed the snapshots of the iso-surface of α_{st} = 0.5 for different B_{max} at t=100 s. The results showed the height of meniscus near the narrow face (x = 0.75 m) decreased with the increasing of B_{max}. Across the mould wide face direction, the meniscus trends to flat as B_{max} was increased: e.g. Fig.9 (a) to (d). This was an indication that the magnetic pressure can flat the meniscus through the proposed method.

The time-averaged (in 5 seconds) outlines of meniscus under different B_{max} were plotted, as showed in Fig.10. In the figure, the y coordinates were plotted on $x - y$ plane at z=0 m ($Left$) and $y - z$ plane at x=0.7 m ($Right$). The results showed that the maximum meniscus height decreased from 2.982 m to 2.955 m (initial height y= 2.95 m) with B_{max} increasing from 0 to 0.05 T. Along the WF direction (x - axis), it was observed that the meniscus outline was flattened as the B_{max} was increased. The results showed that the deformation along the mould NF direction (z - axis) was suppressed as well.

Journal Pre-proof

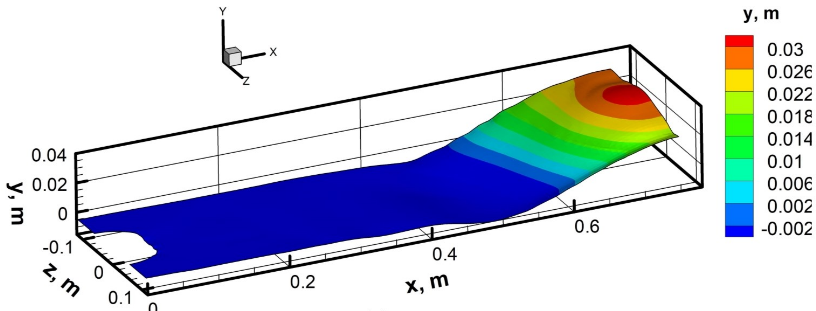

(a) 0 T

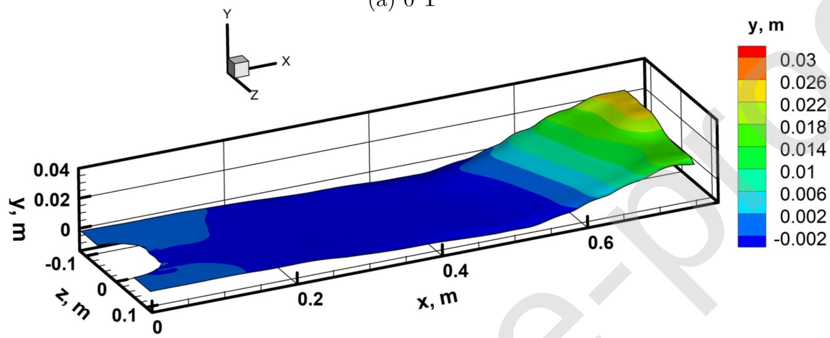

(b) 0.028 T

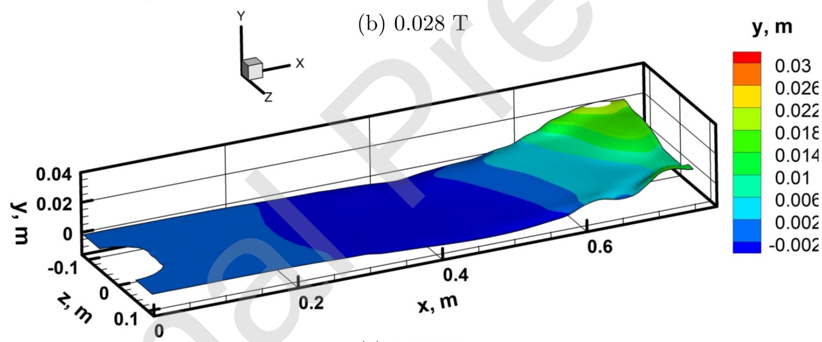

(c) 0.043 T

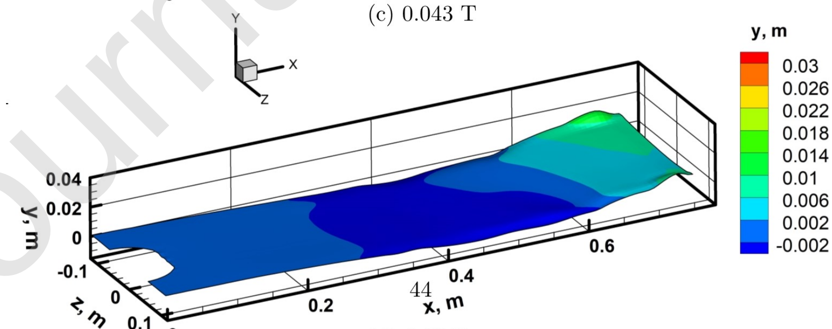

(d) 0.05 T

Figure 9: Three dimensional slag/melt interface shape (plotted on the iso-surface of $\alpha_{st} = 0.5$) under different B_{max} at 100 s. D_{SEN}=0.235 m, θ_p=-15^o and the casting speed is 1.6 m/min. The meniscus is suppressed as B_{max} is increased.

Journal Pre-proof

Journal Pre-proof

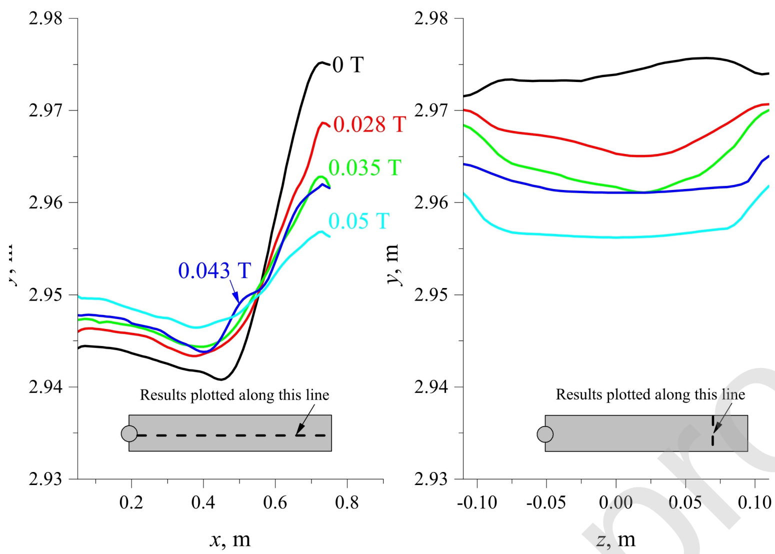

Figure 10: The time-averaged (in 5 seconds) outlines of meniscus under different B_{max}. *Left*: plotted on $x-y$ plane at z=0 m and *Right*: $y-z$ plane at x=0.7 m. The meniscus shape is flattened as B_{max} is increased.

Two methods were adopted to address the meniscus fluctuations. The first method was to use the meniscus height differences (y coordinates difference) at a given time against simulation time. The height difference was defined as Δy:

$$\Delta y = y_{max} - y_{min}, \tag{17}$$

where y_{max} and y_{min} denoted the y coordinates of the highest and the lowest locations of meniscus at the given time. This method was also used by Li et al. (2017) and Hibbeler & Thomas (2010). The Δy variations at different simulation time ($x-y$ plane, $z=0$) was shown in Fig.11. The results showed that the meniscus fluctuation was decreased with the increase of B_{max}. The averaged Δy in the selected time range was decreased from 33.6 to 10.8 mm when B_{max} increased from 0 to 0.05 T. The second method was focusing on a single location and tracking its height with simulation time. Six locations were selected to record meniscus fluctuation and their x coordinates are 0.5, 0.55, 0.6, 0.65, 0.7 and 0.73 m (x=0.75 m is the coordinate of mould narrow face),

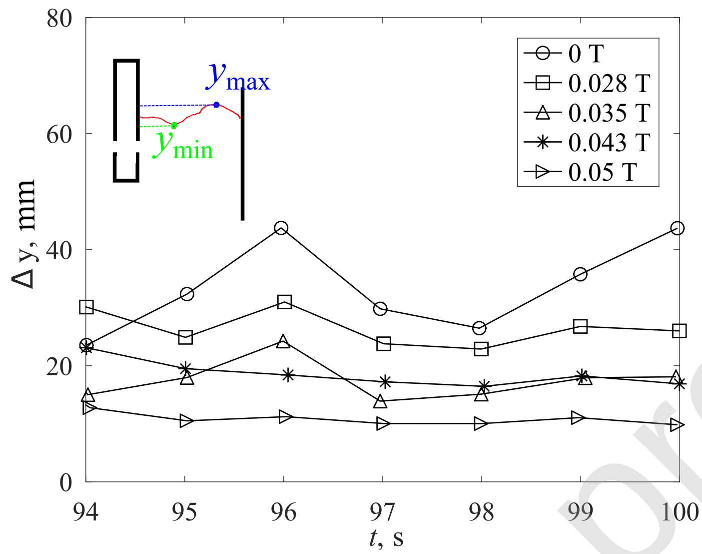

Figure 11: Δy v.s. simulation time. The meniscus fluctuation is suppressed as B_{max} is increased.

respectively. Fig.12 showed the given points' fluctuations with simulation time at different B_{max}. In the figure, y_w was defined as the wave height. $y_w = 0$ referred to the averaged y values between 94 to 100 s on the given point. The results indicated that higher meniscus fluctuations were observed in the vicinity of the narrow face, e.g. x=0.7 m compared to x=0.5 m. This wave was mainly due to the upward flow originated from SEN jet and varied periodically. As B_{max} was increased, this fluctuation was suppressed significantly and this was true for all the selected observing points, which were located from the region near SEN to the narrow face. Fig.13 showed the FFT analysis of meniscus fluctuation signal at $x = 0.73$ and and $z = 0$ m at different B_{max}. The results showed that the applied magnetic field did not change the dominant fluctuation frequency ($f \approx 0.31$ Hz), however, the amplitude of frequency ($|Y(f)|$) was reduced.

Journal Pre-proof

Journal Pre-proof

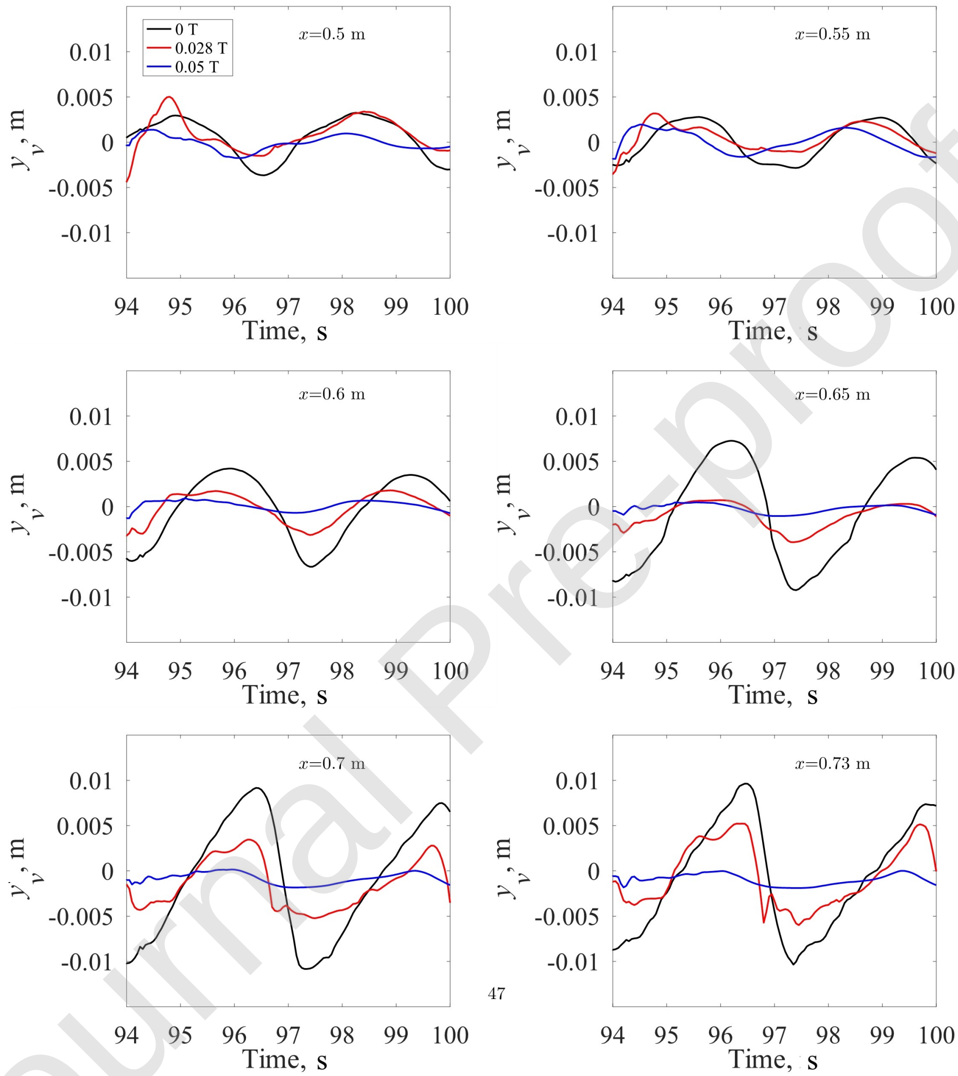

Figure 12: The meniscus fluctuation at a given location (a given x along $x-y$ plane, $z=0$ m) at different B_{max}. For all locations, the fluctuation is reduced as B_{max} is increased. The fluctuation tends to increase as it approaching to the narrow wall of the mould.

Journal Pre-proof

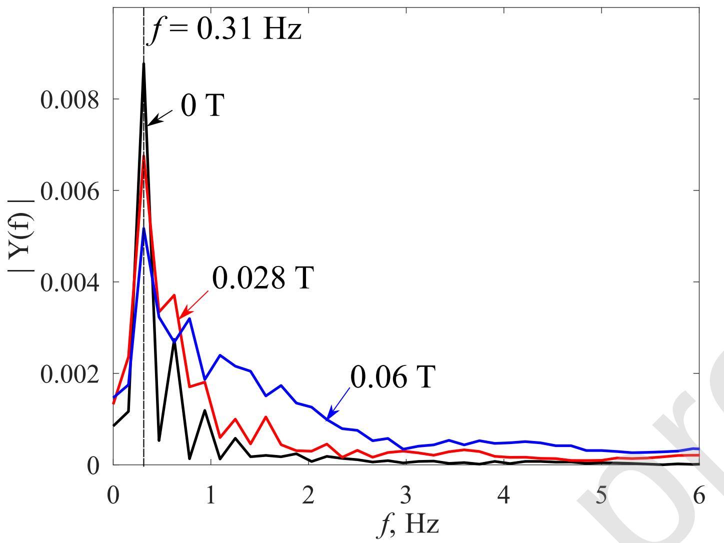

Figure 13: FFT analysis of meniscus fluctuation signal at $x = 0.73$ and and $z = 0$ m at different B_{max}.

4.3. Flow field

315 Fig.14 showed the time averaged surface velocity on the meniscus at different z for different B_{max}. The surface velocity reduces as B_{max} is increased. The location where the maximum velocity appears moves to the NF. Five paths, at different values of z, along the x-axis direction were selected, as plotted in the figure. The results indicated that the maximum velocity is around 0.33 m/s. 320 This velocity magnitude is a reasonable value (Jim et al. (2017)) and slightly higher than suggested optimal surface velocity ranges: higher than 0.1 to 0.2 m/s and less than 0.4 m/s (Kubota et al. (1991)).

Fig.15 showed the contours of the velocity magnitude, velocity x, y and z components at the cases whilst $B_{max} = 0$ (*Left*) and 0.05 T (*Right*) at t=100 s, 325 respectively. The results indicated that the proposed method does not have a significant effect on the flow field underneath the meniscus. However, it was also observed that this method has an affect on the flow across the mould width direction (z). This could be understood as follows. The magnetic pressure

Journal Pre-proof

Journal Pre-proof

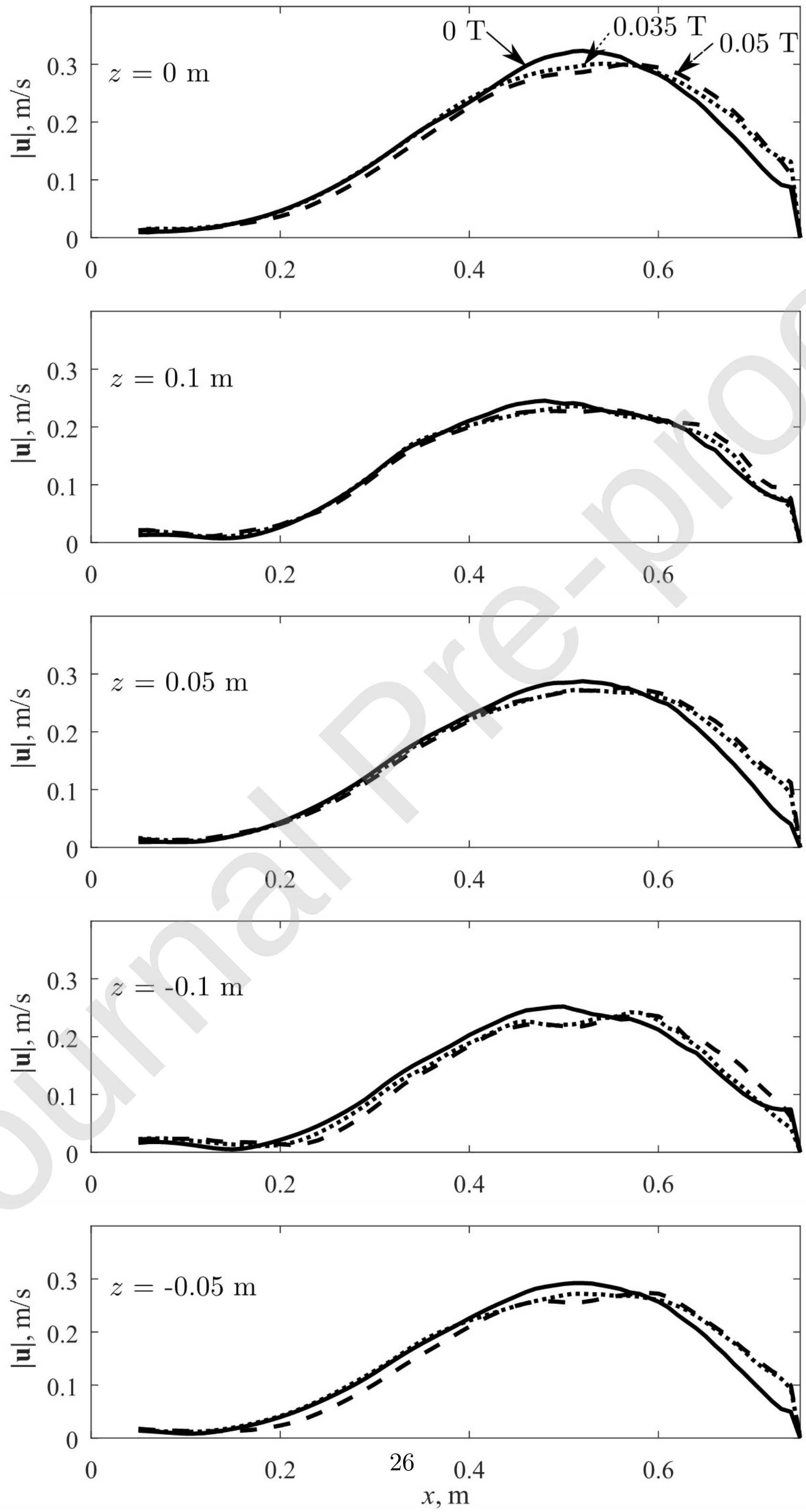

Figure 14: Time averaged surface velocity on the meniscus at different z for different B_{max}. The surface velocity reduces as B_{max} is increased. The location where the maximum velocity appears moves to the NF.

Journal Pre-proof

Journal Pre-proof

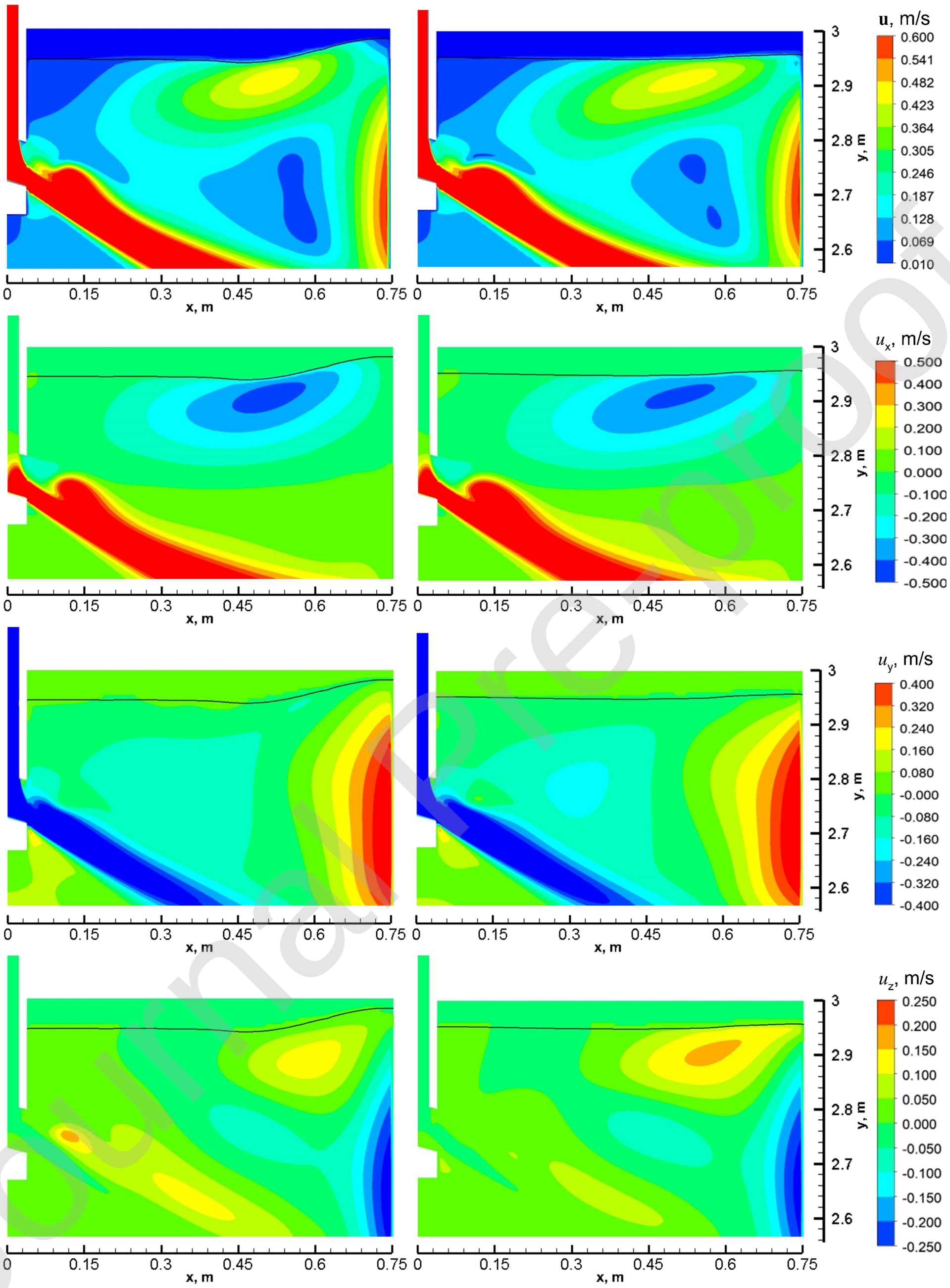

Figure 15: The velocity magnitude and velocity components distribution on the $x-y$ plane at z=0 m at B_{max} = 0 T and 0.05 T at t=100 s.

Journal Pre-proof

suppressed the bulge deformation. The force trended to push the meniscus downwards, towards the casting direction. This part flow met the upward flow originated from the SEN jet, which had a direction towards the meniscus. The meet of two flows with opposite direction will generate a full 'Saddle' point (Weller et al. (1998)). The flow mainstream varies its direction to the wide face of the mould (z) and therefore to increase the velocity z components.

Fig.16 showed the turbulent kinetic energy (TKE) distribution under different magnetic field. The contour was plotted on the $x - y$ plane where z=0 m. The

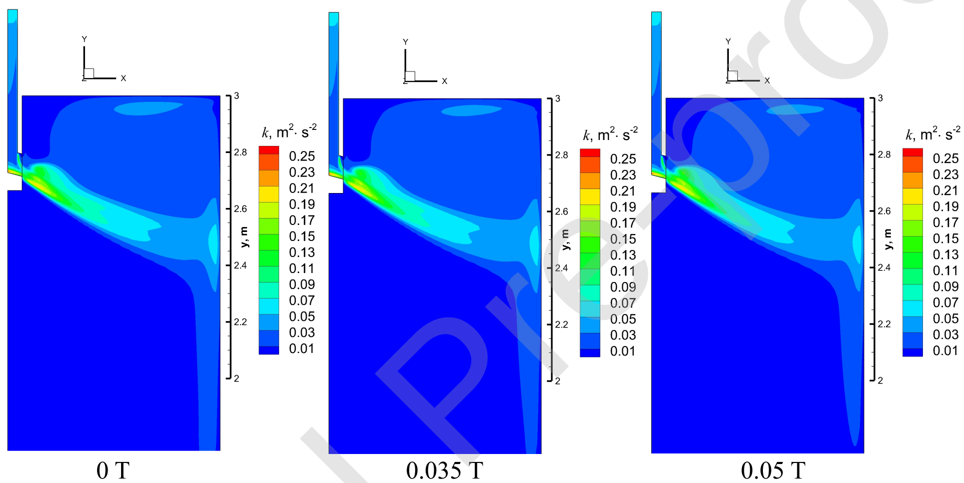

Figure 16: The distribution of turbulent kinetic energy under different magnetic field. The contour was plotted on the $x - y$ plane where z=0 m at t=100 s.

results indicated that the TKE difference is very small in the whole slab mould domain, which is not surprisingly. This is due to the applied magnetic field mainly acts on the meniscus region.

5. Experiment results

The modelling results, discussed in Sec:4, indicated that the proposed magnetic field arrangement can suppress the meniscus fluctuation. In this section, an experiment was designed and conducted as a further validation.

Journal Pre-proof

5.1. Experimental set-up and procedure

Fig.17 showed the experimental facilities and set-up. The low melting point

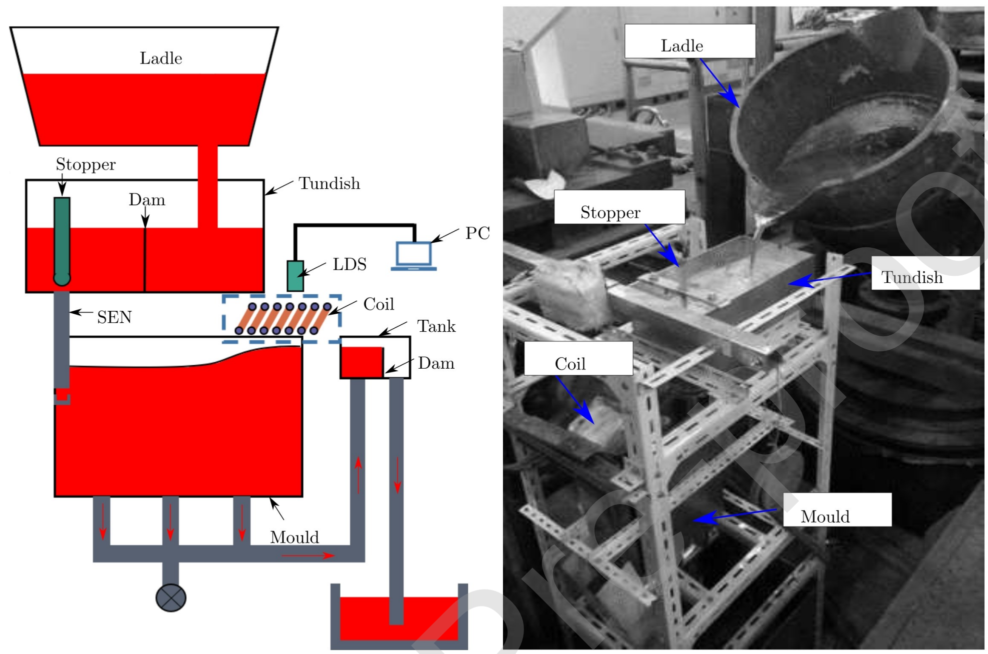

Figure 17: A schematic diagram (front view) and picture of the experiment set-up.

(368 K) alloy (represented by the red colour in Fig.17), Sn (wt pct 20)-Pb (wt pct 30)-Bi, was used to simulate the molten steel. The alloy was melt and poured into the ladle. Then the melt was poured to the tundish. In the tundish, a dam was placed to reduce the impingement effect of jet flow and a stopper was applied for controlling the casting speed (0.55 m/min). A downward port SEN, -10^o, was adopted and the immersion depth of SEN is 0.08 m. The meniscus fluctuation was captured by a laser displacement sensor (Keyence Corporation, Laser Displacement Sensor LK501, 100 Hz). A high frequency (8 kHz) alternating current was applied to the copper coils to generate a high frequency alternating magnetic field (same frequency as the applied alternating current). An 'overflow' tank was adopted to ensure the free level of the melt in the slab mould maintained as the preset level. Tab.3 showed geometric parameters and

Journal Pre-proof

Journal Pre-proof

operating conditions for experiment.

Table 3: Geometric parameters and operating conditions for experiment.

Parameter	Value
Casting temperature, K	523
Casting speed, $m \cdot min^{-1}$	0.55
Operating frequency, kHz	8
Density of SnPbBi, $kg \cdot m^{-3}$	9400
Viscosity of SnPbBi, $kg \cdot m^{-1} \cdot s$	4.2×10^{-2}
Electric conductivity of SnPbBi, $S \cdot m^{-1}$	1.11×10^{6}
Mould dimension (width $\times$ thickness),(mm $\times$ mm)	1500 $\times$ 230
Inner diameter of nozzle, mm	70
Outlet of nozzle (height $\times$ width), (mm $\times$ mm)	80$\times$65
Port angle of SEN (θ_p), deg	-10

The experiment procedures were as follows:

1. To design and manufacture the system;
2. To preheat the low-melting point alloy to 523 K;
3. To pour the melt to the system;
4. To achieve a stable the flow system, e.g. the free surface maintains the pre-set level;
5. To switch on the laser displacement sensor (LDS),
6. To record the meniscus fluctuation. This is the fluctuation result of no applied magnetic field;
7. To switch on the power source and apply AC to I_1 and LDS starts to record. This is the fluctuation result of B^a_{max};
8. To increase the applied AC to I_2 and LDS starts to record. This is the fluctuation result of B^b_{max};
9. Experiment ends.

Journal Pre-proof

5.2. Dimensionless number similarity

To ensure the results obtained from numerical simulation and the experiment are comparable, the Froude number (Fr) and Stuart number (St) should be same. For Fr and St, we have:

$$\frac{|\mathbf{u}|_{ns}^2}{g \cdot L_{ns}} = \frac{|\mathbf{u}|_{exp}^2}{g \cdot L_{exp}}, \tag{18}$$

and

$$\frac{\sigma_{ns} \cdot |\mathbf{B}|_{ns}^2 \cdot L_{ns}}{\rho_{ns} \cdot |\mathbf{u}|_{ns}} = \frac{\sigma_{exp} \cdot |\mathbf{B}|_{exp}^2 \cdot L_{exp}}{\rho_{exp} \cdot |\mathbf{u}|_{exp}}. \tag{19}$$

In the equations, the subscripts ns and exp denote the variables used in the numerical simulation and experiment. $\mathbf{u}$ and L are casting velocity and the reference length of the model. Therefore, the casting velocity and the applied magnetic field can be calculated:

$$|\mathbf{u}|_{ns} = \sqrt{3} \cdot |\mathbf{u}|_{exp}, \tag{20}$$

and

$$|\mathbf{B}|_{ns} = 3^{-0.25} \cdot |\mathbf{B}|_{exp}. \tag{21}$$

The detailed mesh information of the adopted simulation in the figure is identical to the mesh which was given in Fig. 3.

5.3. Experimental results

Fig.18 showed the fluctuations of a given location (x: 1/8 mould wide face length from the narrow face, y: 1/2 mould narrow face and z: at meniscus) under different applied magnetic field. The results indicated that the amplitude of the meniscus fluctuation at the given location is around 2 mm. The fluctuation reduced to 1 mm whilst B_{max}=0.017 T was applied. The results obtained from both experiment and numerical simulation have a good agreement.

6. Conclusion and future work

In this research, we proposed a new type of magnetic field arrangement to suppress the bulged deformation and to reduce the meniscus fluctuation.

Journal Pre-proof

Journal Pre-proof

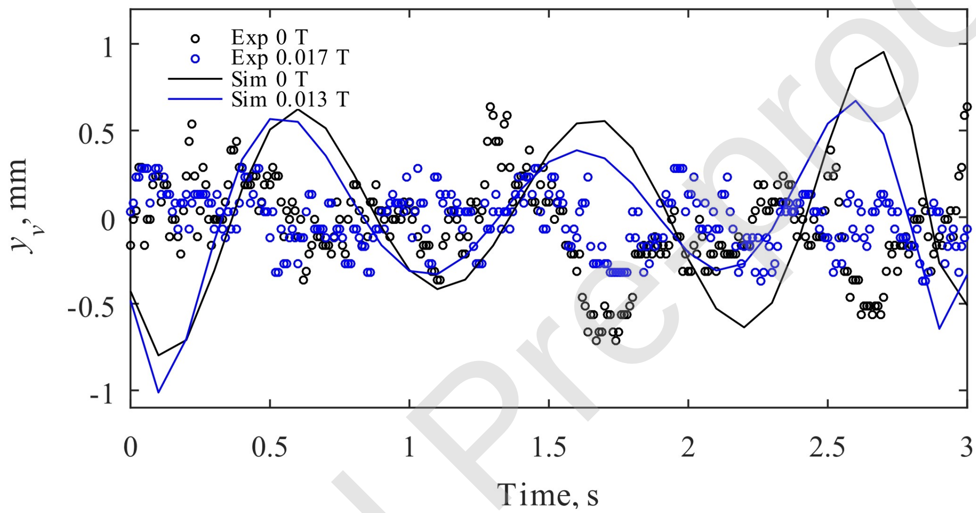

Figure 18: Results of meniscus fluctuation comparison between numerical simulation (solid line) and experiment (dots) at different B_{max}. The meniscus fluctuation is represented by slag/steel interface variations of a given point location (x=0.575 m, y=2.95 m (initial location) and z=0 m, respectively.) with time. The meniscus fluctuation is suppressed whilst the magnetic field is applied for both simulation and the experiments. The amplitudes' reduction has an agreement between the numerical simulation and experiments.

Journal Pre-proof

Journal Pre-proof

The work was conducted through three dimensional (3D) numerical simulations followed by an experiment validation. The main conclusions can be summarized as follows:

1. The proposed method successfully produces the expected magnetic pressure;
2. The bulge deformation was successfully suppressed: the maximum height of meniscus decreases from 32 mm to 5 mm whilst the B_{max} is increased from 0 to 0.05 T;
3. The meniscus trends to flat as B_{max} is increased. The maximum meniscus height difference at a given time decreases from 33.6 to 10.5 mm when the B_{max} is increased from 0 to 0.05 T;
4. For a given location, across the width direction, the fluctuation is also suppressed significantly, as the magnetic field is applied;
5. The velocity on meniscus is not sensitive to the applied magnetic pressure. This is beneficial to ensure the meniscus can maintain a relatively high and uniform temperature to avoid degrade of the final product;
6. The influence of magnetic pressure on the fluid flow underneath the meniscus is small. However, the velocity component along the mould thickness direction is observed to increase;
7. A designed experiment was conducted as a further validation of the proposed method. The experiment results showed agreement with the modelling.

Future work will focus on the second question raised in Sec.1 to figure out what the role played by the Joule heat in the process.

Acknowledgements

This work was supported by National Natural Science Foundation of China (No. 51474065, U1760206) and the 111 Project 2.0 of China (No. BP0719037). The authors would like to thank the reviewers for their work that has contributed to this paper.

Journal Pre-proof

References

References

Armaly, B., Durst, F., Pereira, J., & Schonung, B. (1983). Experimental and theoretical investigation of backward-facing step flow. *Journal of Fluid Mechanics*, *127*, 473–496. doi:https://doi.org/10.1017/S0022112083002839.

Brackill, J., Kothe, D., & C.Zemach (1991). A continuum method for modeling surface tension. *Journal of Computational Physics*, *100*, 335–354. doi:https://doi.org/10.1016/0021-9991(92)90240-Y.

Cho, S., Thomas, B., & Kim, S. (2019). Effect of nozzle port angle on transient flow and surface slag behaviour during continuous steel slab casting. *Metallurgical and Materials Transactions B*, *50*, 52–76. doi:https://doi.org/10.1007/s11663-018-1439-9.

Dousset, V., & Potherat, A. (2008). Numerical simulations of a cylinder wake under a strong axial magnetic field. *Physics of Fluids*, *20*, 017104. doi:https://doi.org/10.1063/1.2831153.

Gupta, D., & Lahiri, A. K. (1994). Water-modelling study of the surface disturbances in continuous slab caster. *Metallurgical and Materials Transactions B*, *25*, 227–233. doi:https://doi.org/10.1007/BF02665205.

Ha, M., Lee, K., & Seong, S. (2003). Numerical simulation of three-dimensional flow, heat transfer and solidification of steel in continuous casting mold with electromagnetic brake. *Journal of Materials Processing Technology*, *133*, 322–339. doi:https://doi.org/10.1016/S0924-0136(02)01009-9.

Hibbeler, L., & Thomas, B. (2010). Investigation of mold flux entrainment in cc molds due to shear layer instability. *AISTech Steelmaking Conference Proc*, (pp. 4–7).

Hwang, Y., Nam, G., Moon, K., & Yoon, J. (1997). Numerical analysis of the influences of operational paramters on the fluid flow and meniscus shape in

Journal Pre-proof

slab caster with embr. *ISIJ International*, *37*, 659–667. doi:https://doi.org/10.2355/isijinternational.37.659.

Jim, K., Vanka, S., & Thomas, B. (2017). Large eddy simulations of the effects of embr and sen submergence depth on turbulent flow in the mold region of a steel caster. *Metallurgical and Materials Transactions B*, *48*, 162–178. doi:https://doi.org/10.1007/s11663-016-0801-z.

Kim, D., Kim, W., & Cho, K. (2000). Numerical simulation of the coupled turbulent flow and macroscopic solidification in continuous casting with electromagnetic brake. *ISIJ International*, *40*, 670–676. doi:https://doi.org/10.2355/isijinternational.40.670.

Kubota, J., Okimoto, K., Shirayama, A., & Murakami, H. (1991). Meniscus flow control in the mold by traveling magnetic field for high speed slab caster. *In Proceedings of the 74th Steelmaking Conference*, (pp. 233–241).

Lehman, A., Talback, G., & Rullgard, A. (1996). Electromagnetic braking improves steel quality in continuous casting. *ABB Review*, *1*, 1–10.

Li, Y., Deng, A., Yang, B., Xu, H., & Wang, E. (2021). Inhibiting bulging deformation of liquid metal free surface by magnetic pressure. *Journal of Iron and Steel Research International*, *28*, 818–829. doi:https://doi.org/10.1007/s42243-020-00468-z.

Li, Z., Wang, E., Zhang, L., Xu, Y., & Deng, A. (2017). Influence of vertical electromagnetic brake on the steel/slag interface behavior in a slab mold. *Metallurgical and Materials Transactions B*, *48*, 2389–2402. doi:https://doi.org/10.1007/s11663-017-1030-9.

Li, Z., Zhang, L., Ma, D., & Wang, E. (2020). Numerical simulation on flow characteristic of molten steel in the mold with freestanding adjustable combination electromagnetic brake. *Metallurgical and Materials Transactions B*, *51*, 2609–2627. doi:https://doi.org/10.1007/s11663-020-01950-5.

Journal Pre-proof

Journal Pre-proof

Miranda, R., Barron, M., Barreto, J., Hoyos, L., & Gonzalez, J. (2005). Experimental and numerical analysis of the free surface in a water model of a slab continuous casting mold. *ISIJ International*, *45*, 1626–1635. doi:https://doi.org/10.2355/isijinternational.45.1626.

Mramor, K., Vertnik, R., & Sarler, B. (2015). A meshless model of electromagnetic braking for the continuous casting of steel. *Materials and technologije*, *49*, 961–967. doi:https://doi.org/10.17222/mit.2015.084.

Negrinia, F., Fabbria, M., Zuccarinia, M., Takeuchib, E., & Tanib, M. (2000). Electromagnetic control of the meniscus shape during casting in a high frequency magnetic field. *Energy Conversion and Management*, *41*, 1687–1701. doi:https://doi.org/10.1016/S0196-8904(99)00185-5.

Singh, R., Thomas, B. G., & Vanka, S. P. (2013). Effects of a magnetic field on turbulent flow in the mold region of a steel caster. *Metallurgical and Materials Transactions B*, *44*, 1201–1221. doi:https://doi.org/10.1007/s11663-013-9877-x.

Spitans, S., Jakovics, A., Bakke, E., & Nacke, B. (2013). Numerical modelling of free surface dynamic of melt in an alternate magnetic field part i: implementation and verification of the model. *Metallurgical and Materials Transactions B*, *44*, 593–605. doi:https://doi.org/10.1007/s11663-013-9809-9.

Sun, X., Li, B., Zhong, Y., Ren, Z., & Lei, Z. (2018). Steel/slag interface behavior under multifunction electromagnetic driving in a continuous casting slab mold. *Metals*, *9*, 983. doi:https://doi.org/10.3390/met9090983.

Thomas, B., Singh, R., Vanka, S., Timmel, K., Eckert, S., & Gerbeth, G. (2015a). Effect of single-ruler electromagnetic braking (embr) location on transient flow in continuous casting. *Journal for Manufacturing Science and Production*, *15*, 93–104. doi:https://doi.org/10.1515/jmsp-2014-0047.

Thomas, B., Singh, R., Vanka, S., Timmel, K., Eckert, S., & Gerbeth, G. (2015b). Effect of single-ruler electromagnetic braking (embr) location on transient flow in continuous casting. *Journal for Manufacturing Science and Production*, *15*, 93–104. doi:https://doi:10.1515/jmsp-2014-0047.

Vertnik, R., Mramor, K., & Sarler, B. (2019). Solution of three-dimensional temperature and turbulent velocity field in continuously cast steel billets with electromagnetic stirring by a meshless method. *Engineering Analysis with Boundary Elements*, *104*, 347–363. doi:https://doi.org/10.1016/j.enganabound.2019.03.026.

Vives, C., & Ricou, R. (1985). Experimental study of continuous electromagnetic casting of aluminum alloys. *Metallurgical and Materials Transactions B*, *16*, 377–384. doi:https://doi.org/10.1007/BF02679730.

Weller, H., Tabor, G., Jasak, H., & Fureby, C. (1998). A tensorial approach to computational continuum mechanics using object-oriented techniques. *Computers in Physics*, *12*, 620–631. doi:https://doi.org/10.1063/1.168744.

Xu, L., Wang, E., Karcher, C., Deng, A., & Xu, X. (2018). Numerical simulation of the effects of horizontal and vertical embr on jet flow and mold level fluctuation in continuous casting. *Metallurgical and Materials Transactions B*, *49*, 2779–2793. doi:https://doi.org/10.1007/s11663-018-1342-4.

Yu, H., Wang, B., Li, H., & Li, J. (2008). Influence of electromagnetic brake on flow field of liquid steel in the slab continuous casting mold. *Journal of Materials Processing Technology*, *202*, 179–187. doi:https://doi.org/10.1016/j.jmatprotec.2007.08.054.

Zhang, L., & Potherat, A. (2013). Influence of the geometry on the two-and three-dimensional dynamics of the flow in a 180 degree sharp bend. *Physics of Fluids*, *25*, 053605. doi:https://doi.org/10.1063/1.4807070.

Journal Pre-proof